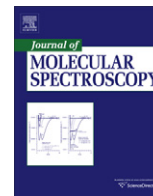




Contents lists available at ScienceDirect

## Journal of Molecular Spectroscopy

journal homepage: www.elsevier.com/locate/jms

NaK bound–free and bound–bound  $4^3\Sigma^+ \rightarrow a^3\Sigma^+$  emissionB.M. McGeehan<sup>1</sup>, S. Ashman<sup>2</sup>, C.M. Wolfe<sup>3</sup>, R. Steinhardt<sup>4</sup>, M.L. Monaco<sup>5</sup>, J. Huennekens, A.P. Hickman\*

Department of Physics, Lehigh University, 16 Memorial Dr. East, Bethlehem, PA 18015, United States

## ARTICLE INFO

## Article history:

Received 16 July 2010

In revised form 11 November 2010

Available online 20 November 2010

## Keywords:

Transition dipole moment function

Bound–free emission

NaK

Excited states

## ABSTRACT

The relative transition dipole moment function  $M(R)$  for the  $4^3\Sigma^+ \rightarrow a^3\Sigma^+$  electronic transition in the sodium–potassium molecule (NaK) has been determined by fitting experimental bound–free and bound–bound emission spectra. The fit is performed using a modified version of the BCONT computer program, which was originally developed by Le Roy. Spectra previously measured in this laboratory from low-lying ro-vibrational levels of the  $4^3\Sigma^+$  state and new spectra from high-lying levels are included in the fit. A slight adjustment to the inner, repulsive wall of the  $4^3\Sigma^+$  potential leads to an improved form for that curve. The fitted  $M(R)$ , when appropriately scaled, agrees very well with recent *ab initio* calculations of Magnier et al.

© 2010 Elsevier Inc. All rights reserved.

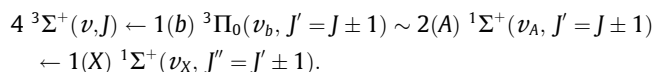
## 1. Introduction

In previous theoretical studies of the  $4^3\Sigma^+ \rightarrow a^3\Sigma^+$  emission in NaK, Magnier et al. [1] found that the transition dipole moment function,  $M(R)$ , exhibited an unusual shape in the region of  $R = 5.3 \text{ \AA}$ , as shown in Fig. 1. By examining emission from low-lying ro-vibrational levels of the  $4^3\Sigma^+$  state, Burns et al. [2] were able to determine experimentally a relative  $M(R)$  for this transition in the range of  $3.8 \text{ \AA} < R < 4.8 \text{ \AA}$ . New emission spectra (reported here) from higher-lying ro-vibrational levels of the  $4^3\Sigma^+$  state provide us with new data to analyze the shape of the  $4^3\Sigma^+ \rightarrow a^3\Sigma^+$  emission. In particular, these new data allow us to fit  $M(R)$  over an extended range of  $R$  that contains the sharp peak shown in previous calculations. Our fits rely on potential energy curves for the initial and final states of the transition. Except where specified otherwise, we use curves for these states that have been reported elsewhere [2–4].

## 2. Experiment

The experimental setup is almost identical to the one described by Burns et al. [2]. Briefly, NaK molecules (in addition to  $K_2$  and  $Na_2$

molecules) are produced in a five-arm heat-pipe oven [5] containing sodium and potassium metal and argon as a buffer gas. The oven is heated to  $\sim 330 \text{ }^\circ\text{C}$ . NaK molecules are excited to specific  $4^3\Sigma^+(v, J)$  levels using a two-step (pump/probe) excitation scheme



In this scheme, the intermediate level is a mixed  $1(b)^3\Pi_0(v_b, J') \sim 2(A)^1\Sigma^+(v_A, J')$  “window” level (where the two components are coupled together by the spin–orbit interaction). The window level is populated from the ground state level by the pump laser, a single-mode cw dye laser (Coherent model 699–29) pumped by a 4 W krypton ion laser. The final upper  $4^3\Sigma^+(v, J)$  level is then populated from the window level by the probe laser, which is a single-mode cw Ti:Sapphire laser (Coherent model 899–29) pumped by a 10 W argon ion laser. Fluorescence from the upper and intermediate levels in the green and red spectral ranges, respectively, is imaged and collected by filtered photomultiplier tubes and these signals are used to set the frequencies of the pump and probe lasers to line centers of the respective transitions. Once the pump and probe laser frequencies are set, resolved bound–free and bound–bound  $4^3\Sigma^+(v, J) \rightarrow 1(a)^3\Sigma^+$  fluorescence is recorded as a function of emission wavelength using a monochromator/photomultiplier combination. The monochromator is a 0.22 m Spex model 1681 used with entrance and exit slits set to  $400 \mu\text{m}$  (resolution  $\sim 1.4 \text{ nm}$ ). A calibrated tungsten–halogen white light source [6] is used to measure the relative detection system efficiency versus wavelength, and all spectra presented in this work have been corrected for this effect.

For  $4^3\Sigma^+$  levels with  $v \geq 12$ , collisions have a tendency to transfer population from the directly excited level to neighboring levels of the  $3^3\Pi$  double minimum state [7]. Unfortunately, the

\* Corresponding author. Fax: +1 610 758 5730.

E-mail addresses: sashman@uwsp.edu (S. Ashman), jph7@lehigh.edu (J. Huennekens), aph2@lehigh.edu (A.P. Hickman).

<sup>1</sup> Present address: Epic Systems Corp., 1979 Milky Way, Verona, WI 53593, United States.<sup>2</sup> Present address: Department of Physics & Astronomy, University of Wisconsin–Stevens Point, Stevens Point, WI 54481, United States.<sup>3</sup> Present address: Army Research Laboratory, RDRL-WMP-A, Aberdeen Proving Ground, MD 21005-5066, United States.<sup>4</sup> Present address: Advanced RF Sensing and Exploitation Group (105), MIT Lincoln Laboratory, 244 Wood St., Lexington, MA 02420, United States.<sup>5</sup> Present address: 27 Taylor Drive, West Caldwell, NJ 07006, United States.

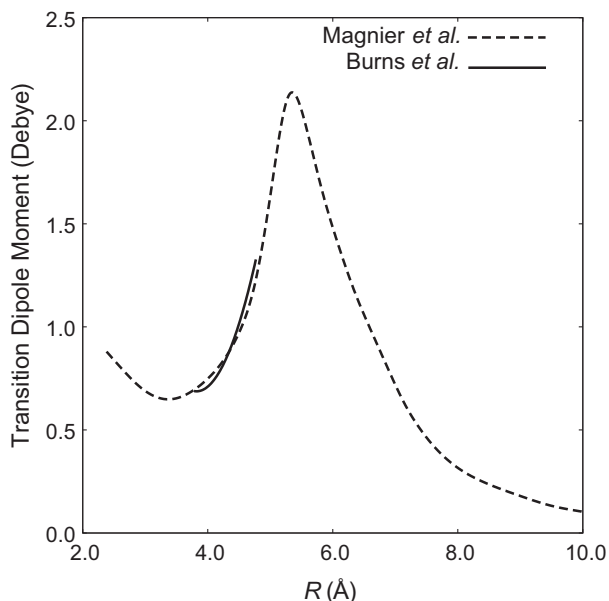


**Fig. 1.** Comparison of previously determined  $4^3\Sigma^+ \rightarrow a^3\Sigma^+$  transition dipole moment functions  $M(R)$ . The dashed curve is the function calculated by Magnier et al. [1]. The solid curve shows the relative values of  $M(R)$  measured by Burns et al. [2] and scaled to the theoretical calculation.

$3^3\Pi$  state also emits strong bound–free fluorescence in the green, and this fluorescence overlaps the  $4^3\Sigma^+(v, J) \rightarrow 1(a)^3\Sigma^+$  fluorescence of interest (see Section 4). This collision-induced  $3^3\Pi$  fluorescence can be reduced relative to the  $4^3\Sigma^+$  fluorescence by lowering the pressure and temperature of the heat-pipe oven, but at the cost of reduced signal-to-noise. Data were recorded with argon buffer gas pressures in the range 0.1–2.0 Torr. In general we found that the best data (least contamination with  $3^3\Pi$  fluorescence) were obtained by reducing the argon pressure to  $\sim 0.1$  Torr and maintaining the temperature near 330 °C. These conditions could only be maintained for relatively short periods of time since this very low argon pressure is not sufficient to confine the alkali vapor and keep it away from the oven windows. All of the new data reported in this paper (initial levels  $13 \leq v \leq 25$ ) were taken under these low pressure conditions.

### 3. Theoretical methodology

We determined the best-fit value of  $M(R)$  by fitting the experimental data using a modified version of the computer program BCONT [8]. One modification was implementing the Levenberg–Marquardt algorithm [9] for the nonlinear least-squares minimization. We used a routine obtained from <http://www.netlib.org> [9] that we have used in many other programs. The other changes, which are described below, were generalizing the form of  $M(R)$  used in the calculations, implementing a convoluting function, and extending the calculation of matrix elements into the bound portion of the final state.

#### 3.1. Form of the transition moment function

We implemented a more general functional form for the transition moment function. For the  $4^3\Sigma^+ \rightarrow a^3\Sigma^+$  transition, we needed different functional forms of  $M(R)$  on either side of the sharp peak shown in Fig. 1. Burns et al. [2] had previously used a quadratic function of  $R$  to fit a relative  $M(R)$  for small  $R$ . Due to the shape of the given  $M(R)$ , it would be difficult to fit  $M(R)$  over the entire

range of  $R$  using a single power series. Thus, we implemented the following functional form for  $M(R)$  for the fit of the data:

$$M(R) = \left[ \sum_{i=1}^n \alpha_i \left( \frac{R - R_0}{R_0} \right)^i \right] S \left( \frac{R - R_x}{w} \right) + \left[ \sum_{j=1}^m \beta_j \left( \frac{1}{R^2} \right)^j \right] \left[ 1 - S \left( \frac{R - R_x}{w} \right) \right]. \quad (1)$$

In this expression, the  $\alpha_i$ 's are the coefficients of a polynomial for the left-hand side of  $M(R)$ , and the  $\beta_j$ 's are the coefficients of a different polynomial for the right-hand side;  $R$  is the internuclear separation distance,  $R_0$  is fixed at 4.2 Å, the approximate equilibrium separation of the  $4^3\Sigma^+$  state, and  $S$  is a switching function. The switching function allows for a smooth transition from one power series to the other and is expressed as

$$S(y) = \begin{cases} 1 - \frac{1}{2} \exp \left[ - \left( y - \frac{1}{\sqrt{2}} \right)^2 + \frac{1}{2} \right] & \text{if } y < 0 \\ \frac{1}{2} \exp \left[ - \left( y + \frac{1}{\sqrt{2}} \right)^2 + \frac{1}{2} \right] & \text{if } y \geq 0. \end{cases} \quad (2)$$

The argument of  $S$  in Eq. (1) is

$$y = \frac{R - R_x}{w}, \quad (3)$$

so that  $R_x$  is the switching point, and  $w$  is related to the width of the region in which the switch occurs. As shown in Fig. 2,  $S(y)$  varies smoothly from 1 to 0 over a range of about three units in  $y$  centered about the point  $y = 0$ . The first, second, and third derivatives of  $S(y)$  are continuous at the point  $y = 0$ .

#### 3.2. Convolution function

We simulated the spectral broadening due to monochromator resolution by implementing a convoluting function that is triangular in shape. The convoluted intensity at a given wavelength  $\lambda_n$  is the weighted average of the calculated intensities at the  $2N + 1$  (equally spaced) wavelengths  $\lambda_i$ , for  $i = n - N, \dots, n + N$ . The value of  $N$  is related to the ratio of the FWHM of the instrumental resolution to  $\Delta\lambda$ , the spacing of the experimental data points, and the weights are proportional to the area of a thin band of the triangle function [10]:

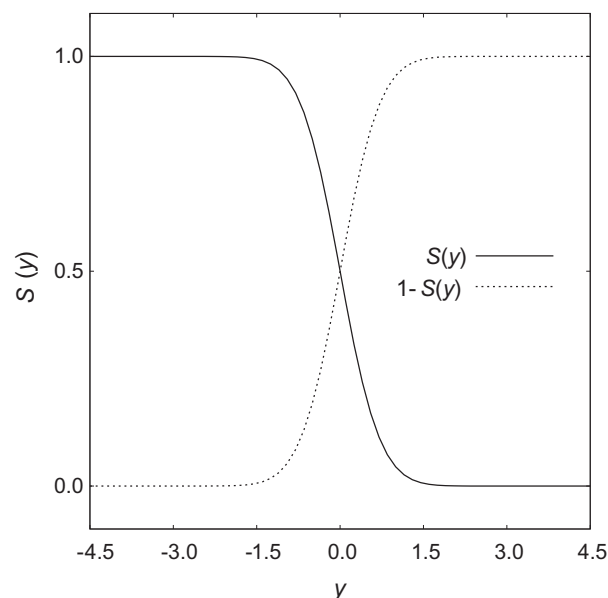


**Fig. 2.** The switching function  $S(y)$  defined by Eq. (2).

$$\zeta_i = \begin{cases} \frac{4(N+i)+2}{(2N+1)^2} & \text{if } -N \leq i \leq -1 \\ \frac{4N+1}{(2N+1)^2} & \text{if } i = 0 \\ \frac{4(N-i)+2}{(2N+1)^2} & \text{if } 1 \leq i \leq N. \end{cases} \quad (4)$$

Typical values of  $N$  for this work were in the range 10–25.

### 3.3. Bound-free and bound-bound calculations

While most of the experimental data used in our calculations correspond to bound-free emission, a small portion of the data, typically at shorter wavelengths, involves the emission arising from bound-bound transitions. These discrete lines are sufficiently broadened by the monochromator that they cannot be individually resolved. However, by including these data in the fit, we were able to obtain a relative transition moment function that extends to larger  $R$  and provides a more stringent test of the theoretical work [1].

We first calculate the bound-free matrix elements  $\zeta_{\nu',E}$ , which determine the number of transitions per second per molecule  $\zeta_{\nu',E}dE$  from an initial vibrational state to a final state whose energy is between  $E$  and  $E + dE$ :

$$\zeta_{\nu',E}dE = \frac{64\pi^4\nu^3}{3hc^3} \left| \int \chi_E(R)M(R)\chi_{\nu'}(R)dR \right|^2 dE. \quad (5)$$

In this expression,  $\chi_E(R)$  is the energy-normalized continuum wavefunction [11] of the  $a^3\Sigma^+$  state,  $\chi_{\nu'}(R)$  is the initial  $4^3\Sigma^+$  bound state wavefunction, and  $M(R)$  is the transition dipole moment function. We calculate  $\zeta_{\nu',E}$  on a grid of points corresponding to the experimental transition energies. Next, we calculate the bound-bound matrix elements,  $\zeta_{\nu',\nu''}$ , which give the number of transitions per second between an initial vibrational state and a final vibrational state,

$$\zeta_{\nu',\nu''} = \frac{64\pi^4\nu^3}{3hc^3} \left| \int \chi_{\nu''}(R)M(R)\chi_{\nu'}(R)dR \right|^2. \quad (6)$$

In this expression,  $\chi_{\nu''}(R)$  is the bound, lower state wavefunction, and  $\chi_{\nu'}(R)$  is again the initial state wavefunction. Allison and Dalgarno [12] showed that the product of  $\zeta_{\nu',\nu''}$  defined in Eq. (6) and the density of states  $d\nu/dE$  of the  $a^3\Sigma^+$  electronic potential gives a function of energy  $\zeta_{\nu',\nu''}d\nu/dE$  that smoothly joins  $\zeta_{\nu',E}$  at the boundary between bound-bound and bound-free spectra.

To determine the density of states of the  $a^3\Sigma^+$  electronic potential, we use near dissociation expansion (NDE) theory [13,14]. For a potential of the form

$$V(R) = D_e - C_n/R^n, \quad (7)$$

where  $D_e$  is the dissociation limit, Le Roy and Bernstein [13] showed that

$$E(\nu) = D_e - [(v_D - \nu)H_n]^{2n/(n-2)}, \quad (8)$$

where  $H_n$  is a collection of constants depending on  $C_n$ , and  $v_D$  is the noninteger value for the vibrational index of the dissociation limit. Specializing to the present case of  $n = 6$  and rearranging terms, we can transform Eq. (8) to the form

$$\nu = v_D - z/H_6, \quad (9)$$

where  $z$  is a reduced binding energy of level  $\nu$ :

$$z = [D_e - E(\nu)]^{1/3}. \quad (10)$$

Comparat [14] later showed how to include additional terms in Eq. (8) to describe bound-state energies further from the dissociation

limit. His work provides justification for a more general polynomial form for  $\nu$  as a function of  $z$ .

We did find that the vibrational quantum number  $\nu$  was a very smooth function of the reduced binding energy  $z$  for the calculated energies of the bound portion of the  $a^3\Sigma^+$  potential. Fig. 3 shows the results. The highest vibrational states are well fit by the linear form of Le Roy and Bernstein [13], and the lower states are well fit by higher order terms, as suggested by Comparat [14]. One can write the density of states  $d\nu/dE$  in terms of  $d\nu/dz$  using the chain rule:

$$\frac{d\nu}{dE} = -\frac{1}{3}[D_e - E(\nu)]^{-2/3} \frac{d\nu}{dz}. \quad (11)$$

We used cubic spline interpolation of the points shown in Fig. 3 to evaluate  $\nu(z)$  and then  $d\nu/dz$ .

It should be noted that the NDE is only rigorous for electronic potentials with no rotational contribution. For our study, the experimental spectra used do not satisfy this condition. As a result, we have replaced the dissociation limit,  $D_e$ , with the top of the rotational barrier,  $D'$ , in Eq. (11). This method provides good fits of the calculated energies, as shown in Fig. 3, so that we were able to determine  $d\nu/dE$  using Eq. (11). However, the reviewer of this manuscript suggested an alternate method of calculating  $d\nu/dE$  based on the WKB approximation. We investigated this method and found very good agreement with the fitting method originally used. The details of the WKB method are available in (see Supplementary material).

## 4. Results and discussion

In order to calculate the bound-free and bound-bound  $4^3\Sigma^+ \rightarrow a^3\Sigma^+$  emission, we needed to specify the potentials used in the calculation. For the initial  $4^3\Sigma^+$  state, we used the experimentally determined potential of Burns et al. [2]. For the final  $a^3\Sigma^+$  state we used the previously determined repulsive wall [4] and bound portion of the potential well [3]. Using these potentials, we obtained preliminary fits of the experimental data by only

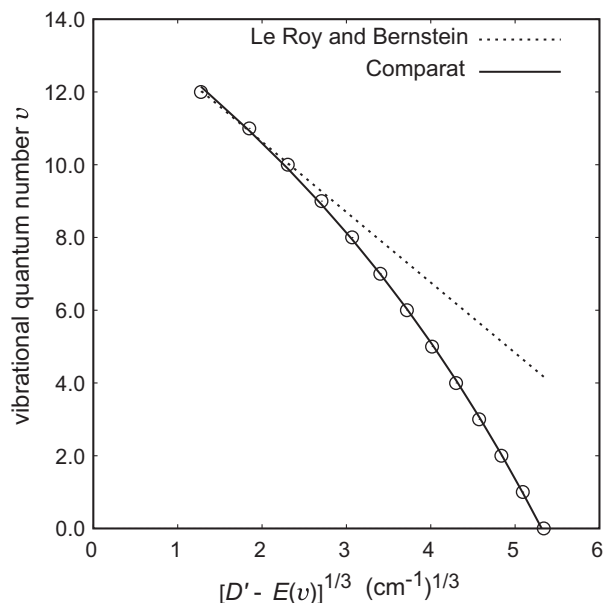
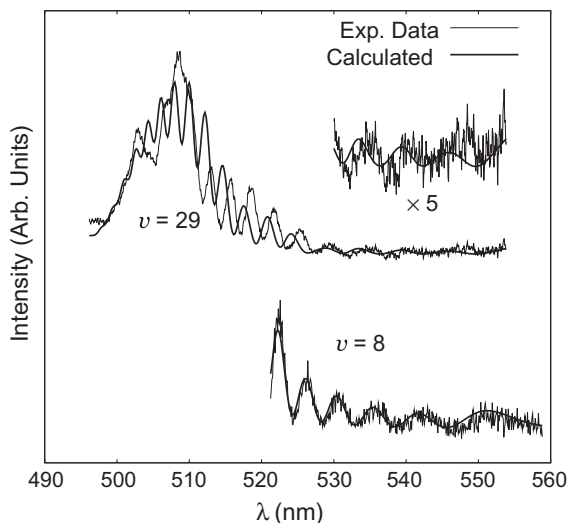


Fig. 3. Reduced plot of the energy levels ( $\circ$ ) of the  $a^3\Sigma^+$  state of NaK with  $J = 36$ . The dashed line shows the fit of the three highest energy levels using the result of Le Roy and Bernstein [13], and the solid line shows the fit of all of the energy levels using the higher order term proposed by Comparat [14]. As discussed in Section 3.3 in the text,  $D'$  is the energy of the rotational barrier of the potential.



**Fig. 4.** Comparison between initial calculations and experiment for the  $4\ 3\Sigma^+ \rightarrow a\ 3\Sigma^+$  emission spectra. The calculation for  $\nu = 8$  agrees well with the experimental data, but the calculation for  $\nu = 29$  has two noticeable differences. The first is that the peaks in the calculated spectrum at longer wavelengths are slightly shifted to the left. Also, the number of peaks at the short wavelength region of the calculated spectrum is not consistent with the experimental data.

considering bound–free emission. The comparisons with experimental data for two of the states we used in the fit are shown in Fig. 4. The calculations agree well with the experimental data for  $\nu = 8$ , as shown in the figure, and also for all lower values of  $\nu$ . However, two major discrepancies are present in the fit for  $\nu = 29$  (shown in the figure) and other vibrational levels for  $\nu \geq 13$ . The first is that the peaks in the calculation at longer wavelengths are not at the same positions as the corresponding peaks in the data. Secondly, at shorter wavelengths, the number of peaks in the calculation does not match the number of peaks in the experimental spectrum.

We first considered the offset of the calculated peaks at longer wavelengths. For the peaks to shift to longer wavelengths, either the repulsive wall of the lower state would have to be more repulsive or the repulsive wall of the initial state would have to be less repulsive. We found that for small adjustments for  $R < 3.3\ \text{\AA}$  in the lower state repulsive wall determined by Ferber et al. [4], no noticeable shift in the calculated peaks occurred. We then considered a small modification to the  $4\ 3\Sigma^+$  state. Using the IPA method [15], we started with a slightly modified wall, and then iteratively adjusted the entire potential to obtain the best fit to the rovibrational energy levels. For  $R$  less than an attachment point  $R_1$ , the initial guess for the modified repulsive wall used the following functional form, which matches the original potential and its derivative at  $R_1$ :

$$\tilde{V}(R) = V(R_1) + \frac{dV}{dR}(R_1) \frac{1 - \exp[-\lambda_1(R - R_1) + \lambda_2(R - R_1)^2]}{\lambda_1}, \quad (12)$$

where  $V(R)$  is the electronic potential determined by Burns et al. [2], and  $\lambda_1$  and  $\lambda_2$  are adjustable parameters. Using initial values  $R_1 = 3.8896\ \text{\AA}$ ,  $\lambda_1 = 0.39771\ \text{\AA}^{-1}$  and  $\lambda_2 = 0.7\ \text{\AA}^{-2}$ , we obtained convergence of the IPA method to a potential very similar to the original potential of Burns et al. [2]. Fig. 5 presents a comparison of these two potentials. The two potentials fit the  $4\ 3\Sigma^+$  bound states with comparable accuracy, and the present potential leads to closer agreement between the calculations and the experimental peaks in the bound–free and bound–bound spectrum. A table of the two IPA potentials for the  $4\ 3\Sigma^+$  state is available in (see Supplementary material).

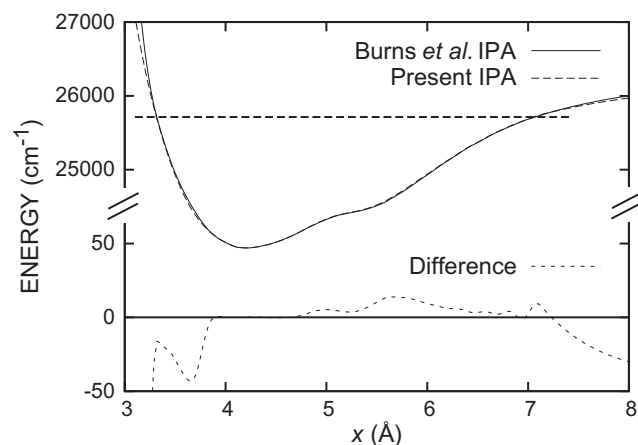


**Fig. 5.** Comparison of the IPA potentials determined by Burns et al. [2] and in the present work. The difference is also shown, by a factor of 20 relative to the potentials. The difference is less than  $0.2\ \text{cm}^{-1}$  near the bottom of the well. The horizontal dashed line crossing the potential curves marks the approximate location of the highest bound states that were included in the fit. At points less than this energy, the new potential has a maximum shift towards the left of  $0.02\ \text{\AA}$ .

Next we considered the discrepancy at shorter wavelengths between the number of calculated peaks and the number of observed peaks. Fig. 4 shows broad peaks in the experimental data for  $\nu = 29$  at wavelengths  $\lambda \approx 503$  and  $508\ \text{nm}$ . The calculated spectrum exhibits several peaks in the same region. In fact, the measured spectra for  $\nu = 13, 16, 20$ , and  $25$  all exhibit only two peaks in this wavelength region. We concluded that this double peak feature is a result of bound–free emission from the  $3\ 3\Pi$  state of NaK, which is populated by collisions. Comparison of the location of the observed peaks with those observed in Ref. [7] led to this conclusion. To provide additional evidence that this extraneous signal was arising from collisions, the spectroscopic data for bound–free emission from the  $4\ 3\Sigma^+$  state was taken at several pressures for  $\nu = 13, 16, 20$ , and  $25$ . Fig. 6 shows examples of these spectra. The experimental and calculated peaks at longer wavelengths are normalized to the same height; it is clear that the signal from the  $3\ 3\Pi$  state at  $\lambda \approx 503$  and  $508\ \text{nm}$  becomes smaller relative to the longer wavelength  $4\ 3\Sigma^+$  emission as the pressure is decreased. In order to reduce the influence of the  $3\ 3\Pi$  emission, we have used the data

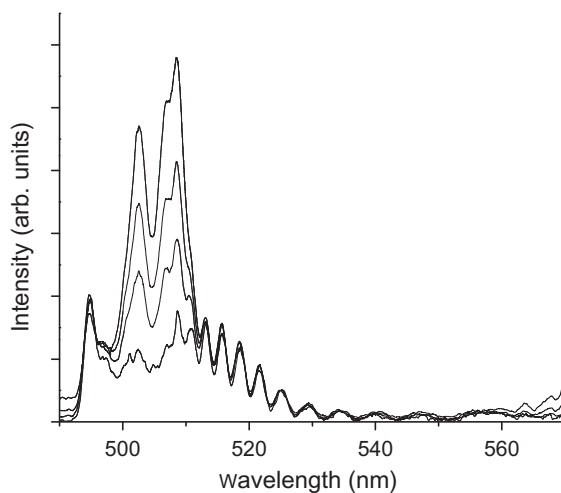


**Fig. 6.** Argon buffer gas pressure dependence for the NaK  $4\ 3\Sigma^+(\nu = 25, J = 16) \rightarrow 1(a)\ 3\Sigma^+$  bound–bound and bound–free emission. The curves from top to bottom show the collision-induced  $3\ 3\Pi \rightarrow 1(a)\ 3\Sigma^+$  emission at  $P_{\text{Ar}} = 2.0, 1.0, 0.5$  and  $0.1\ \text{Torr}$ , respectively. The temperature is  $T \sim 330\ ^\circ\text{C}$ . All curves are normalized to each other at  $\lambda = 525\ \text{nm}$ .

recorded at the lowest possible pressure consistent with a reasonable signal-to-noise ratio. We have also included the uncertainty of the data in the fitting procedure and assigned a large uncertainty to the data in this region. Despite these procedures, the large probability of collisional transfer to the  $3^3\Pi$  state made it impossible to obtain spectra uncontaminated by the  $3^3\Pi$  emission. Similar ubiquitous collisional transfer to the  $2^3\Pi_g$  states of homonuclear alkali diatomics has been observed [16–20].

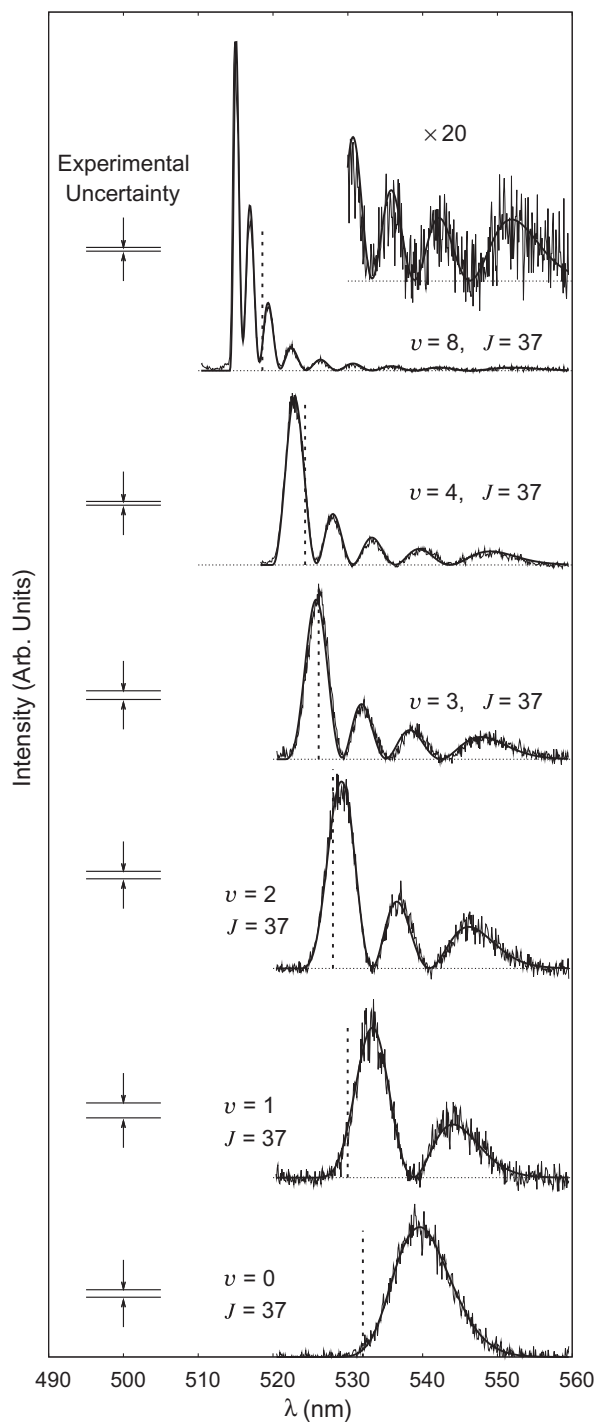


**Fig. 7.** Comparison of calculated emission spectra with the data of Burns et al. [2]. The thick lines represent the calculations; the thin lines represent the experimental data. The vertical dashed lines separate the bound-free (on the right) and the bound-bound emission spectra (on the left). The inclusion of the bound-bound calculations allows us to fit the data to smaller wavelengths, yielding two additional peaks for  $v = 8$ .

#### 4.1. Improved calculated emission spectra

Now we present the calculated intensities for the  $4^3\Sigma^+ \rightarrow a^3\Sigma^+$  transitions, including bound-free and bound-bound emission. We consider 10 initial states. Six of these states are the same ones used by Burns et al. [2], namely  $v = 0-4$ , and 8, all with  $J = 37$ . The remaining four states are those recently obtained with  $(v, J) = (13, 37), (16, 14), (20, 14),$  and  $(25, 16)$ . Using emission scans corresponding to those 10 states, and including the bound-bound

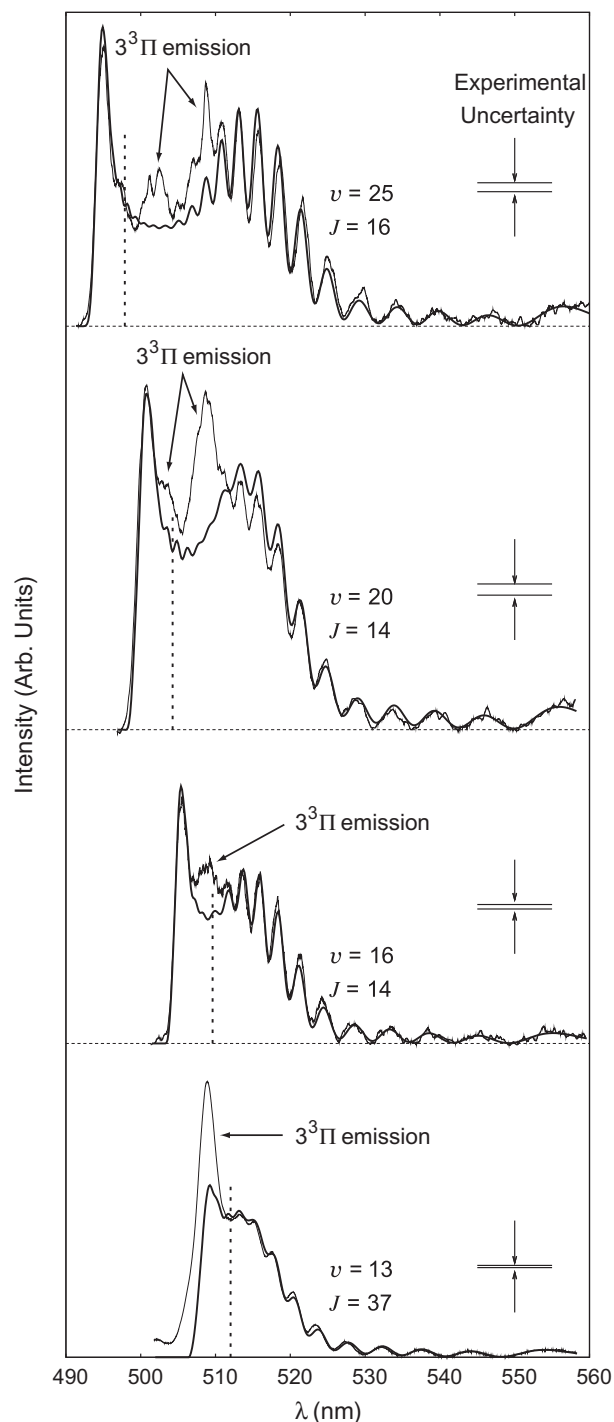


**Fig. 8.** Comparison of calculated emission spectra with new data for high vibrational levels of the  $4^3\Sigma^+$  state. The conventions are the same as in Fig. 7. The calculations match the experimental data within the experimental uncertainty except where the spectra are contaminated by collision-induced  $3^3\Pi$  emission.

emission in the analysis, we could fit the emission spectra at smaller transition wavelengths, where bound–bound transitions occur, and we also obtained a better fit of the  $4^3\Sigma^+ \rightarrow a^3\Sigma^+$  transition dipole moment function.

Figs. 7 and 8 show the calculated emission spectra, including both the bound–bound and bound–free emission. The vertical line in these figures denotes the separation point between the purely bound–free spectra (to the right of the vertical line) and the bound–bound spectra (to the left of the line). As can be seen in the figures, the calculated spectra yield more information in the short wavelength region when the bound–bound emission is included in the calculations, particularly for the initial ro-vibrational levels with higher vibrational quantum numbers.

#### 4.2. Improved transition moment function

The relative transition dipole moment function  $M(R)$  determined by fitting both the bound–free data and the bound–bound data is shown in Fig. 9. The function that gives the best fit is given by the solid line, and dashed lines show a range of possible functions that yield acceptable fits to the spectroscopic data. It is clear from the figure that the new spectroscopic data reported here dramatically extend the range of  $R$  that has been probed. A new  $M(R)$  has been determined for values of  $R$  from 3.5 to 6.5 Å. The new function matches the previous work of Burns et al. [2] and (when appropriately scaled) is also in excellent agreement with the prediction of Magnier et al. [1].

We now discuss the method used to estimate the uncertainties in the fitting parameters and the bounds presented in Fig. 9. The dipole moment function that we use is specified by Eq. (1) and has five adjustable parameters. (Only four parameters are independent. The experimental spectra we fit are not absolute, so the overall normalization is arbitrary.) Three of the parameters ( $\alpha_0$ ,  $\alpha_1$ , and  $\alpha_2$ ) are used in the power series expansion of  $R$ . One of the remain-

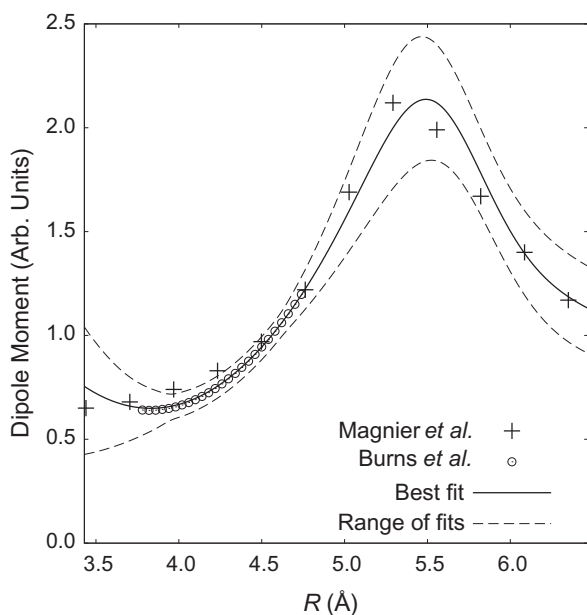


**Fig. 9.** The range of transition dipole moment functions that yield acceptable fits to the experimental spectra for the  $4^3\Sigma^+ \rightarrow a^3\Sigma^+$  transition of NaK. The (+) symbols show the points calculated by Magnier et al. [1], and the circles show the function determined experimentally by Burns et al. [2]. The allowed functions calculated by this work are bounded by the dashed curves, and the solid line shows the best fit transition moment function. Note that these fits yield only a relative transition dipole moment function. The fitted curves are normalized to the calculated dipole moment of Magnier et al.

**Table 1**

Coefficients for the relative transition dipole moment function obtained from fitting the bound–bound and bound–free portions of the experimental data, and the absolute uncertainties associated with each parameter.

Variable parameters	Best fit value	Uncertainty
$\alpha_0$ (Debye)	0.82	$\pm 0.06$
$\alpha_1$ (Debye)	2.3	$\pm 0.8$
$\alpha_2$ (Debye)	13	$\pm 7$
$\beta_1$ (Debye Å <sup>2</sup> )	52	$\pm 10$
$R_x$ (Å)	5.59	$\pm 0.11$
Fixed parameters		Value
$R_0$ (Å)	4.2	
$w$ (Å)	0.5	

ing terms,  $\beta_1$ , is used in the power series expansion of  $1/R^2$ . We initially used another parameter,  $\beta_2$ , but it did not significantly improve the fit, and so we dropped it. The other remaining term is the switching position  $R_x$ . Although we could have let the width of the switching function ( $w$ ) vary, we found that setting it equal to 0.5 Å was better. When it was allowed to vary, it would become unreasonably small, typically less than the spacing between points of the calculation grid, or less than 0.0015 Å, leading to dipole moment functions that appeared physically unreasonable.

We estimated the uncertainties in the parameters by assessing the relation between the quality of the fit and the value of the statistical quantity  $\chi^2$ , which is defined [20] as

$$\chi^2 = \sum_{i=1}^{N_p} \left( \frac{y_{\text{calc},i} - y_{\text{exp},i}}{u_{\text{exp},i}} \right)^2, \quad (13)$$

where  $N_p$  is the number of data points,  $y_{\text{calc},i}$  and  $y_{\text{exp},i}$  are the calculated and experimental data points, respectively, and  $u_{\text{exp},i}$  is the experimental uncertainty.

We performed a series of calculations in which one fitting parameter (say  $\alpha_1$ ) was fixed at a value  $\Delta\alpha_1$  greater or less than its best-fit value, and the other parameters were re-optimized. By varying  $\Delta\alpha_1$ , we concluded that the quality of the fit was not seriously compromised if the value of  $\chi^2$  increased by less than 5%. We used this guideline to obtain the uncertainties for each fitting parameter that are displayed in Table 1. We also examined the functions  $M(R)$  determined when each fitting parameter was fixed at its minimum and maximum values (and the others optimized). The largest and smallest values for all the possible functions  $M(R)$  thereby obtained determine the dashed lines in Fig. 9.

#### 5. Concluding remarks

We have determined the dipole moment function  $M(R)$  for the  $4^3\Sigma^+ \rightarrow a^3\Sigma^+$  electronic transition in NaK by fitting experimental bound–free and bound–bound emission spectra. Recent theoretical calculations [1] predicted that this  $M(R)$  would exhibit sharp structure near 5.3 Å, and the present work confirms that prediction. The present determination of  $M(R)$ , which relies partly on newly-measured spectra from the  $\nu = 13\text{--}25$  states of the  $4^3\Sigma^+$  electronic state, is also completely consistent with a previous determination [2] of  $M(R)$  for  $R \leq 4.8$  Å.

#### Acknowledgments

This work was supported by the National Science Foundation Grant Nos. PHY-0652938 and PHY-0968898. RS and MM were supported by NSF REU site Grant No. PHY-0849416. APH and BMM acknowledge helpful correspondence with D. Comparat.

## Appendix A. Supplementary data

Supplementary data associated with this article can be found, in the online version, at [doi:10.1016/j.jms.2010.11.004](https://doi.org/10.1016/j.jms.2010.11.004).

## References

- [1] S. Magnier, M. Aubert-Frécon, Ph. Millié, J. Mol. Spectrosc. 200 (2000) 96–103.
- [2] P. Burns, L. Sibbach-Morgus, A.D. Wilkins, F. Halpern, L. Clarke, R.D. Miles, Li Li, A.P. Hickman, J. Huennekens, J. Chem. Phys. 119 (2003) 4743–4754.
- [3] K. Ishikawa, N. Mukai, M. Tanimura, J. Chem. Phys. 101 (1994) 876–881.
- [4] R. Ferber, E.A. Pazyuk, A.V. Stolyarov, A. Zaitsevskii, P. Kowalczyk, H. Chen, H. Wang, W.C. Stwalley, J. Chem. Phys. 112 (2000) 5740–5750.
- [5] C.R. Vidal, J. Cooper, J. Appl. Phys. 40 (1969) 3370–3374.
- [6] R. Stair, W.E. Schneider, J.K. Jackson, Appl. Opt. 2 (1963) 1151–1154.
- [7] L. Morgus, P. Burns, R.D. Miles, A.D. Wilkins, U. Ogba, A.P. Hickman, J. Huennekens, J. Chem. Phys. 122 (2005) 144313.
- [8] R.J. Le Roy, G.T. Kraemer, BCONT 2.1: A Computer Program for Calculating Bound → Continuum Transition Intensities for Diatomic Molecules, Chemical Physics Research Report No. CP-650R, University of Waterloo, 2002. <<http://leroy.uwaterloo.ca/programs.html>>.
- [9] B.S. Garbow, K.E. Hillstrom, J.J. More, 1980. <<http://netlib.org/minpack/lmdif1.f>>.
- [10] B. McGeehan, Investigation of Bound-Free Emission Spectra of NaK, Ph.D. Thesis, Lehigh University, Unpublished, 2010.
- [11] F. Mies, J. Chem. Phys. 48 (1968) 482–494.
- [12] A.C. Allison, A. Dalgarno, J. Chem. Phys. 55 (1971) 4342–4344.
- [13] R.J. Le Roy, R.B. Bernstein, J. Chem. Phys. 52 (1970) 3869–3879.
- [14] D. Comparat, J. Chem. Phys. 120 (2004) 1318–1329.
- [15] A. Pashov, W. Jastrzębski, P. Kowalczyk, Comp. Phys. Commun. 128 (2000) 622–634.
- [16] A. Kopystyńska, P. Kowalczyk, Opt. Commun. 28 (1979) 78–80.
- [17] M. Allegrini, L. Moi, Opt. Commun. 32 (1980) 91–95.
- [18] C. Radzewicz, P. Kowalczyk, J. Krasieński, Z. Phys. A – Atoms Nuclei 314 (1983) 293–296.
- [19] S. Milošević, P. Kowalczyk, G. Pichler, J. Phys. B 20 (1987) 2231–2238.
- [20] J.T. Bahns, W.C. Stwalley, G. Pichler, J. Chem. Phys. 90 (1989) 2841–2847.
- [21] W.H. Press, B.P. Flannery, S.A. Teukolsky, W.T. Vetterling, Numerical Recipes (FORTRAN), first ed., Cambridge University Press, Cambridge, MA, 1989.